Journal of Materials Chemistry A

COMMUNICATION

View Article Online
View Journal | View Issue

Cite this: J. Mater. Chem. A, 2019, 7, 14496

Received 11th March 2019
Accepted 28th May 2019

DOI: 10.1039/c9ta02640a

rsc.li/materials-a

Single-cluster Au as an usher for deeply cyclable Li metal anodes†

Tingzhou Yang, [ab] Tao Qian, *[a] Xiaowei Shen, [a] Mengfan Wang, [a] Sisi Liu, [a] Jun Zhong, [c] Chenglin Yan *[a] and Federico Rosei *[b]

The practical application of lithium (Li) metal anodes is limited by various issues, especially the uncontrolled growth of dendrites. Herein, we report single-cluster Au uniformly dispersed on activated carbon cloth as a model to control directed Li deposition and suppress Li dendrite growth. Single-cluster Au can induce Li plating with zero nucleation overpotential, due to an optimized electron field distribution, as validated by DFT calculations. Stable and reversible Li metal anodes were achieved by virtue of single-cluster Au, exhibiting excellent cycling stability for more than 900 cycles with almost 100% coulombic efficiency and deeply cyclable behavior at a high areal capacity of up to 20 mA h cm^{-2}. Benefiting from guided Li deposition and maximum Li-utilization, we found that Li metal batteries with high-loading cathodes also deliver an outstanding electrochemical performance, showing promise for future rechargeable Li metal battery technologies.

Introduction

High energy and cost-effective Li-ion batteries are promising for large-scale energy storage applications such as electric vehicles, consumer electronics and grid energy storage. However, traditional Li-ion batteries are approaching their theoretical energy density limits.[1–4] In this context, Li metal anodes are ideal candidates due to their low redox potential (−3.04 V *vs.* the standard hydrogen electrode) and high theoretical specific energy (3860 mA h g^{-1}).[5–11] Unfortunately, the uncontrolled formation of dendrites, the large volume change and the unstable interface during electrochemical cycling hinder the applications of Li metal anodes, which reduce the cycling life and lead to safety hazards including internal short circuits and thermal runaway.[12–16] Several strategies have been investigated to address these issues, yet oriented control over Li deposition remains elusive.[8–14,17] The systematic investigation of Li nucleation behavior has become particularly relevant to spontaneously guide Li deposition with control over both morphology and position. The nucleation overpotential is defined as the difference between the bottom of the voltage dip and relatively stable voltage platform, which is induced by heterogeneous Li nucleation and mass-transfer resistance.[18–20] The mass-transfer overpotential is used to trigger Li ion migration on the collector's surface, connected with the current density and the process of Li ion migration in the electrolyte. The heterogeneous nucleation overpotential is necessary for the deposition of Li metal on a heterogeneous electrode, which is affected by the lithiophilicity of the electrode surface. Different materials exhibit varying overpotential values, resulting from their respective thermodynamic behaviours toward Li metal. For a conventional collector, the nucleation overpotential of C, Ni and Cu is around 15–40 mV, which is too high to overcome nucleation barriers.[19]

Noble metals have been widely used in several areas of technology, including pharmaceuticals, environmental protection, catalysts and energy storage.[21–28] It is noteworthy that the nucleation overpotential on noble metals is essentially zero, which can cause Li ions to selectively nucleate on the noble metals and be spatially controlled on anode substrates.[18–20] Unfortunately, noble metals are scarce and expensive, and are very unreactive in the bulk state, limiting their potential for commercial use. Downsizing noble metals to single clusters or atoms can effectively decrease their usage and maximize the atom efficiency.[25–28] However, previous theoretical studies showed that these singly dispersed atoms or clusters would be thermodynamically unstable. To date, significant progress has been achieved in the development of tightly bound single clusters or atoms by strong electronic or covalent interactions.

[a]College of Energy, Soochow University, Suzhou 215006, China. E-mail: tqian@suda.edu.cn; c.yan@suda.edu.cn

[b]Institut National de la Recherche Scientifique, Centre Énergie, Matériaux et Télécommunications, 1650 Boulevard Lionel Boulet, J3X 1S2 Varennes, Québec, Canada. E-mail: rosei@emt.inrs.ca

[c]Institute of Functional Nano and Soft Materials (FUNSOM), Jiangsu Key Laboratory for Carbon-Based Functional Materials and Devices, Soochow University, Suzhou 215123, China

† Electronic supplementary information (ESI) available. See DOI: 10.1039/c9ta02640a

As a noble metal, Au has been demonstrated to effectively enhance electrocatalytic activity by favorable local interfacial interactions. Single-cluster Au, in unsaturated coordination environments, is usually more reactive than the corresponding particle and cluster counterparts, which are more selective to a specific product.[24–26] Due to the infinite surface free energy, quantum size effects and strong metal–support interaction, single-cluster Au will make a breakthrough in the limitation of shallow cycling conditions, and realize the potential of deeply cyclable Li metal electrodes.

Herein, we report the dispersion of single-cluster Au on activated carbon cloth (SCAu-CC) as a model to guide Li deposition uniformly, thereby constraining the growth of dendrites. Single-cluster Au not only favors Li deposition with zero overpotential similar to Au nanoparticles, but also has great affinity and interactions with Li ions in the electrolyte, providing stable adsorption positions for Li atoms, which are further confirmed by density functional theory (DFT) calculations. After being supported by single-cluster Au, the Li anodes can maintain a good plating/stripping efficiency of 99.82% for 900 cycles at 1 mA h cm^{-2}, and be deeply cycled at a high current density and areal capacity of 15.0 and 20.0 mA h cm^{-2} with a high coulombic efficiency. Moreover, Li metal batteries (LMBs) are successfully assembled, and show high Li-utilization and feasibility of the anodes.

Experimental section

Preparation of single-cluster Au dispersed on activated carbon cloth

Carbon cloth was washed and dried thoroughly before the experiments. After this, the carbon cloth was treated using a modified Hummers method. Single-cluster Au was dispersed on activated carbon cloth using a typical three-electrode cell consisting of a working electrode, a platinum counter electrode, and an Hg/HgO reference electrode in a mixture of 0.05 M NaCl and 0.3 mM $HAuCl_4$. Single-cluster Au was deposited on activated carbon cloth by stepping the potential to −0.6 V *vs.* SCE for 5 s, followed by stepping back to −0.2 V *vs.* SCE for 5 s for six cycles.

Structural characterization

The morphologies and elemental mapping were studied using field emission scanning electron microscope imaging and field emission transmission electron microscopy using a SU8010, Hitachi, Ltd and a FEI Tecnai $G^2$20, FEI NanoPorts, Ltd. Subangstrom-resolution aberration-corrected scanning transmission electron microscopy (STEM, FEI Titan ETEM G2 80-300) was used to characterize the dispersion and configuration of single clusters. Surface elemental analysis was performed using X-ray photoelectron spectroscopy (XPS, Kratos Axis Ultra DLD, Japan) and X-ray powder diffraction (XRD, D8 ADVANCE, Bruker AXS GmbH Co., Ltd). X-ray absorption near edge structure (XANES) and extended X-ray absorption fine structure (EXAFS) data were collected on beamline 14W at the Shanghai Synchrotron Radiation Facility (SSRF) and on beamline 01C at the Taiwan Light Source (TLS).

Electrochemical measurements

CR2032-type coin cells were employed in an argon-filled glove box for repeated plating and stripping testing and Li foil was used as the counter/reference electrode. The electrolyte was 1 M lithium hexafluorophosphate ($LiPF_6$) in ethylene carbonate (EC)/diethyl carbonate (DEC) (1 : 1 by volume). For symmetric batteries, two alkali metal anodes using various current collectors were reassembled into CR2032-type coin cells with 80 μL electrolyte and a Celgard separator. The batteries were first treated by an activated process *via* galvanostatic cycling between 0.01 and 1.0 V at 0.5 mA cm^{-2} for 5 cycles to remove surface contamination and form a primordial SEI layer. Then, a fixed amount of Li was plated onto the substrates and stripped when charging to 1.0 V during each cycle. For metal batteries, the SCAu-CC-Li (with a Li loading of 8 mA h cm^{-2}) anodes were obtained from preprocessed symmetric cells. Metal batteries with Li foil were assembled with $LiFePO_4$, respectively. The $LiFePO_4$ electrodes were prepared by mixing active materials, polyvinylidene fluoride, and carbon black in the ratio 8 : 1 : 1 with *N*-methyl-2-pyrrolidone as the solvent. The areal mass loading of the $LiFePO_4$ electrodes was ~12 mg cm^{-2}.

Computational details

First principles calculations in the framework of density functional theory, including structural and electronic performances, were carried out based on the Cambridge Sequential Total Energy Package known as CASTEP. The exchange-correlation functional under the generalized gradient approximation (GGA) with norm-conserving pseudopotentials and the Perdew–Burke–Ernzerhof functional was adopted to describe the electron–electron interaction. An energy cutoff of 750 eV was used and a *k*-point sampling set of 5 × 5 × 1 was tested for convergence. A force tolerance of 0.01 eV $Å^{-1}$, an energy tolerance of 5.0 × 10^{-7} eV per atom and a maximum displacement of 5.0 × 10^{-4} Å were considered. Each atom in the storage models was allowed to relax to the minimum in the enthalpy without any constraints. The vacuum space along the *z* direction is set to be 15 Å, which is enough to avoid interactions between two neighboring images. Then, the Li atom had been adsorbed on the surface of graphite, and graphite + Au. Bonding energy ΔE_{bond} of the Au atom on the surface of substrates is defined as

$$\Delta E_{bond} = E_{*Au} - (E_{*} + E_{Au}) \quad (1)$$

where *Au and * denote the adsorption of the Au atom on substrates and the bare substrates and E_{Au} denotes the chemical potential of Au element. Adsorption energy ΔE of Li group on the surface of substrates is defined as

$$\Delta E = E_{*Au} - (E_{*} + E_{A}) \quad (2)$$

where *A and * denote the adsorption of the Li atom on substrates and the bare substrates and E_A denotes the chemical potential of the Li element.

Results and discussion

Single-cluster Au was supported on the carbon skeleton, and was characterized by scanning electron microscopy (SEM), transmission electron microscopy (TEM) and aberration-corrected high-angle annular dark-field scanning transmission electron microscopy (HAADF-STEM). As shown in Fig. 1a and S1, S2,† after the introduction of single-cluster Au, the structure of the skeleton shows no significant change and Au particles are not detected. HAADF-STEM images show that the bright spots corresponding to single-cluster Au are uniformly dispersed on the skeleton (Fig. 1b). Meanwhile, electron energy-loss spectroscopy (EELS) mapping images of SCAu-CC suggest that atomic Au distributes evenly on the surface of the carbon skeleton (Fig. 1c and S3†). The chemical state and crystal structure of single-cluster Au were further investigated by X-ray photoelectron spectroscopy (XPS) (Fig. S4a†) and X-ray diffraction (XRD) (Fig. S4b†). Fig. S4a† shows the XPS survey spectrum of SCAu-CC. The peak representing Au 4f is clearly visible in the spectra, while the XRD peaks of Au on SCAu-CC almost disappear in the curve compared with those of Au particles-CC. These observations indicate that the Au distributes on the carbon cloth in the form of single clusters.

Normalized X-ray absorption near edge structure (XANES) spectra for Au L_3-edges of PAu-CC and SCAu-CC are shown in Fig. 1d with comparison to standard Au foil, which were further used to investigate the local electronic structure and their interaction with the carbon skeleton. The spectrum of the Au foil and PAu-CC exhibits almost no white-line intensity, due to the completely filled 5d state of Au^0. The white-line intensity of SCAu-CC marked by arrows increases substantially, suggesting that more electrons transfer from the Au cluster to the carbon skeleton. The variation of intensity is consistent with that of the Au–O coordination number, further demonstrating that the electronic properties of Au could be dramatically improved by forming unique atomic scale Au structures. Fig. 1e shows extended X-ray absorption fine structure (EXAFS) data. The peaks at 2.14 Å and 2.56 Å are associated with Au–Au peaks, which are obvious in the Au foil and PAu-CC spectra. The intensity of the peaks decreases due to the formation of unique nanoscale or atomic scale structures. The Fourier transforms of SCAu-CC show one prominent peak at 1.84 Å from the Au–O contribution and a weak peak at 2.53 Å from either the Au–C or Au–Au contributions. Compared with the Au foil and PAu-CC, the significant intensity of Au–O bonds and considerable deviation of the Au–Au bonds indicate the presence of single-cluster Au.

The magnitude of the nucleation overpotential for Li deposition on the collector is particularly relevant for island growth and evolution of surface morphology.[29,30] From Fig. 2a, the nucleation overpotential of metallic Li plating on Cu foil is about ~46 mV, and CC exhibits a nucleation overpotential of

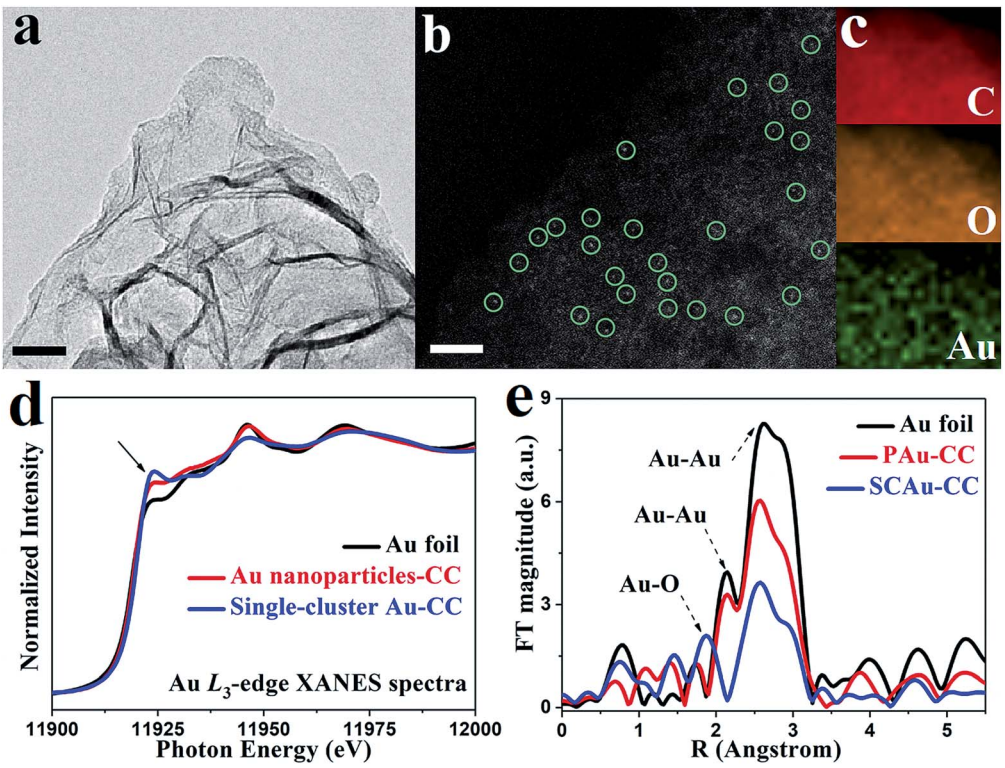

Fig. 1 Morphology and characteristics of SCAu-CC. (a) TEM images of SCAu-CC. Scale bar, 50 nm. (b) HAADF-STEM image of SCAu-CC, and single-cluster Au is highlighted in green circles. Scale bar, 2 nm. (c) Examination of the corresponding EELS mapping of C, O, and Au reveals the homogeneous distribution of single-cluster Au on the carbon skeleton. (d) Au L_3-edge XANES spectra of the samples. (e) Fourier-transformed k^3-weighted extended X-ray absorption fine structure (EXAFS) spectra.

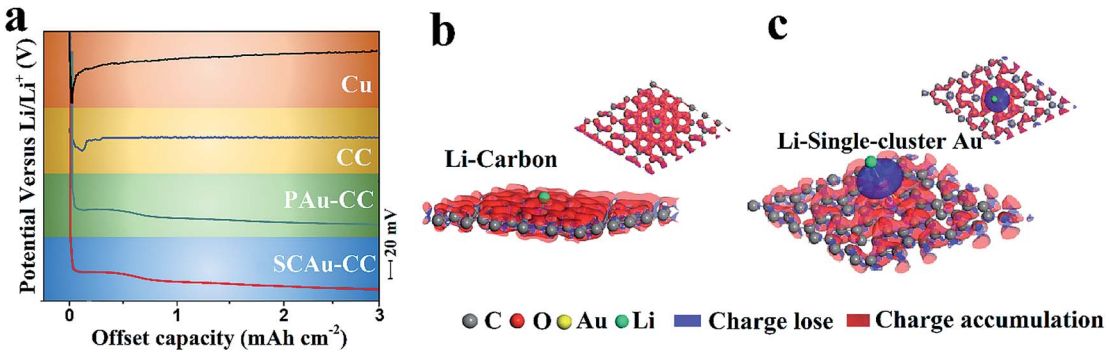

Fig. 2 Demonstration of the strong interaction between single-cluster Au and Li metal. (a) Voltage profiles of galvanostatic Li deposition on Cu foil, CC, PAu-CC and SCAu-CC. Electron density distribution and binding energy of the stable configurations with (b) Li atoms adsorbed on the carbon skeleton, and (c) Li atoms adsorbed on SCAu-CC.

~13 mV. Driven by the electric field, Li ions transfer toward the collector's surface and start nucleating. The nucleation sites for Li plating are randomly distributed and isolated due to the high nucleation overpotential of the collector. After nucleation, the voltage maintains relatively stable values. This suggests that subsequent Li ions will be more inclined to nucleate on previous sites, leading to the growth of dendrites. By contrast, SCAu-CC and PAu-CC exhibit a similar Li metal nucleation behavior to the Au electrode. The Li metal nucleation overpotential on the SCAu-CC collector is essentially 0 mV, which could conveniently guide Li to deposit on even-distributed single-cluster Au, offering uniform nucleation sites (Fig. S5†). The decrease of the nucleation overpotential after dispersing single-cluster Au on the CC collector implies that the Au interface sites play a vital role in Li plating behavior, in agreement with the results of DFT calculations.

The interaction between single-cluster Au and Li atoms, electron density distribution and binding energy were further used to demonstrate that Li nucleation is induced by single-cluster Au, which promotes the selective and uniform deposition of Li metal on the skeleton. Electrophilic Li ion diffusion is slower than electron transfer and the distribution process is stochastic. The morphology of Li metal deposition mainly depends on the distribution and diffusion of Li ions near the surface of the current collector. Fig. 2b shows that the charge distribution is homogeneous on the bare CC collector. This means that Li ions remain scattered throughout the carbon skeleton, which will cause an uneven accumulation of Li metal. In addition, the binding energy between the Li atoms and carbon skeleton is only 0.14 eV. Such values are extremely weak and imply that the Li cluster can easily detach from the bare CC collector, resulting in the growth of Li dendrites and isolated Li particles ("dead Li"). By contrast, for SCAu-CC, single-cluster Au with maximum reactivity is uniformly distributed on the surface of the whole carbon skeleton. As shown in the center of Fig. 2c the π electrons of the carbon skeleton tend to accumulate in the region around Au atoms, and single-cluster Au with Li atoms exhibits a relatively large binding energy of 0.52 eV. Therefore, the charge localization and strong interactions of Au atoms effectively enhance the affinity for Li ions and guide Li ion deposition, realizing spatial control over Li nucleation. In addition, Au can react with Li to generate multiple Li_xAu alloy phases, which will be beneficial for Li deposition on Au with zero overpotential. Induced by the uniform single-cluster Au nanoseeds, Li ions are only selectively deposited on the surface of SCAu-CC, where no amplified and uncontrolled Li deposition occurs, maintaining a dendrite-free morphology.

Seeded growth of Li metal on single-cluster Au with uniform distribution can form a well-regulated Li anode in the collector, as proved from the SEM images of the anodes after Li deposition on different collectors at 6 mA h cm^{-2}. For the bare CC and PAu-CC collector, obvious Li clustering and a rough surface can be seen on the collectors (Fig. S6a–d†), which grows vertically outside the collectors. The uncontrolled growth of Li dendrites without constraint and spatial confinement will cause an internal short circuit of the Li metal battery, with obvious safety concerns. By contrast, from the SEM images of SCAu-CC in Fig. S6e and f,† no apparent pancake-like Li pieces are observed on the surface of the carbon skeleton, which is uniformly covered by a layer of smooth Li without recognizable Li dendrites. The successful plating of Li was further characterized by XRD measurements and the cross-section view of SEM images. Broad and strong peaks at around 44° and 26° correspond to the (002) and (100) crystal planes of carbon substrates (Fig. S7a†). In addition, the peaks located at 36° (100), 52° (200) and 65° (211) are observed, which is in accordance with the characteristic peaks of bare Li foil. More importantly, as shown in the cross-sectional view (Fig. S7b†), the surface of carbon skeletons, especially for the interior 3D skeletons, is uniformly encapsulated by the Li deposit layer with an average thickness of ~1.25 μm. The structural integrity of SCAu-CC after Li plating remained well preserved, indicating superior flexibility and robust mechanical properties. To further illustrate the efficient suppression of Li dendrite growth and directed uniform Li plating, we used *in situ* optical microscopy to record the dynamic process of Li deposition. For the bare CC collector, protrusions and dendrites start to appear along the edges, and become more and more obvious over time (Fig. 3a, and Video†). As shown in Fig. S8,† some Li filaments still grow on the edge of the PAu-CC collector during the Li plating process, and the

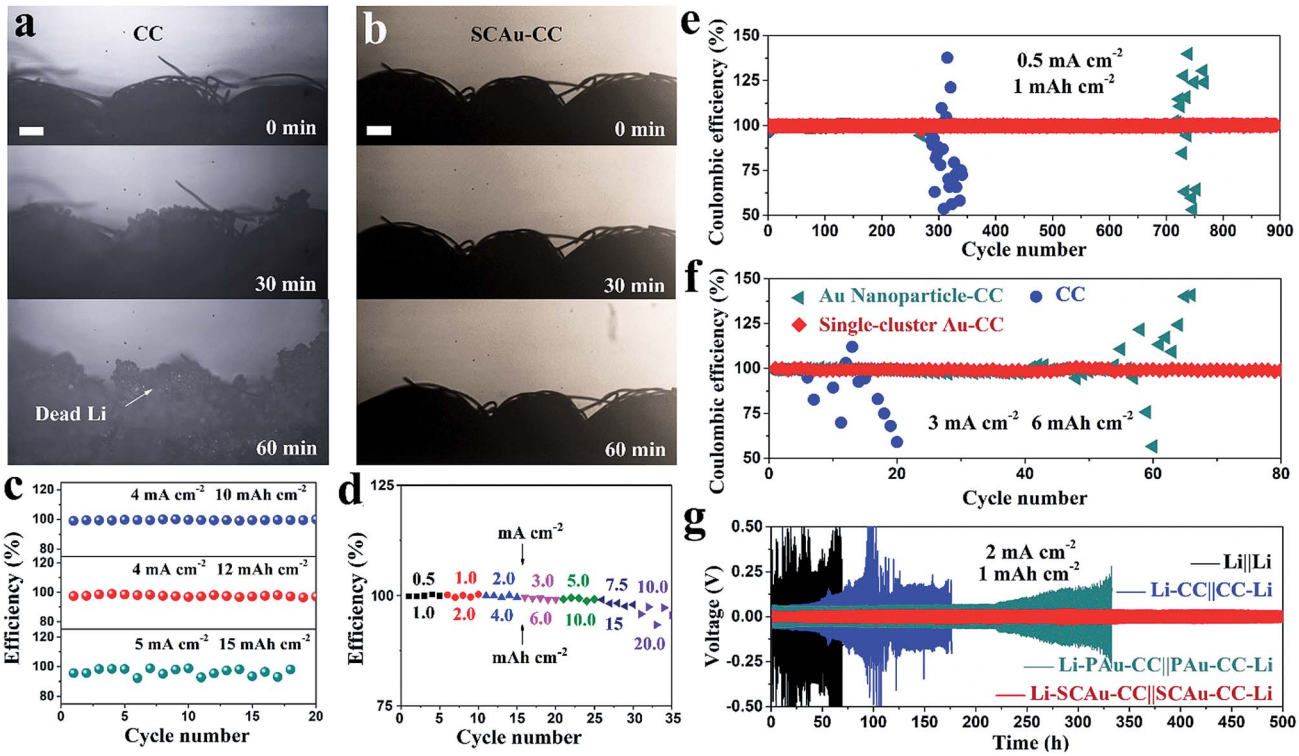

Fig. 3 Electrochemical behaviour of Li metal batteries. *In situ* optical microscopy observations of the Li deposition process with (a) CC and (b) SCAu-CC. (c) CE of the SCAu-CC electrode at 10.0–15.0 mA h cm^{-2}. (d) Rate capability of the CE at different areal capacities from 1.0 to 20 mA h cm^{-2}. Comparison of the CE of Li plating/stripping at a current density of (e) 0.5 mA cm^{-2} and (f) 3.0 mA cm^{-2} with an areal capacity of 1.0 mA h cm^{-2} and 6.0 mA h cm^{-2}, respectively. (g) Cycling performance of different symmetric cells at a current density of 2.0 mA cm^{-2} for more than 500 h.

carbon skeleton is filled with mossy Li. In contrast, Li metal selectively nucleates on uniform single-cluster Au with a negligible nucleation overpotential, and the edge of the SCAu-CC collector remains smooth, free from pulverization and Li dendrites (Fig. 3b), according to the SEM images and electrochemical performance.

The morphologies of the SCAu-CC electrode are further examined by SEM at different points of Li stripping during cycling. As shown in Fig. S9,† Li dendrites and dead Li are present during the whole Li stripping process for the PAu-CC and CC substrates. In sharp contrast, the surface of SCAu-CC at different points during the first Li stripping process remains smooth without dendritic and mossy Li. Furthermore, the obvious variation can also be observed from the XRD patterns of Li-SCAu-CC after Li stripping at different points. The intensity of the Li (100) plane gradually decreases and finally vanishes as the stripping process goes on, demonstrating the successive removal of Li deposits from the 3D carbon skeleton. Such observations confirm the superior reversibility during the Li plating/stripping process. It is well known that the high coulombic efficiency during testing under cycling conditions is attributed to the excellent reversibility of the SCAu-CC electrode, and the SEM images of electrodes after different Li stripping processes are presented as further stronger evidence for the high coulombic efficiency (Fig. S10†).[16–18] The obvious Li dendrites and dead Li can be seen on the surface of PAu-CC and CC even at the end of the first Li striping process. In sharp contrast, the edge of the SCAu-CC electrode remains smooth after Li stripping, free from pulverization and Li dendrites. The XRD pattern of corresponding electrodes is displayed in Fig. S11.† No signal corresponding to the Li deposits can be observed in the XRD pattern of the SCAu-CC electrode, regardless of different cycles of the Li plating/stripping process. However, the peaks located at 36° (100), 52° (200) and 65° (211) are observed for PAu-CC and CC electrodes even after the first Li stripping process, which demonstrated vestigial Li dendrites and dead Li.

Coulombic efficiency (CE) is defined as the ratio between Li stripping and Li plating capacity during cycling of Li metal batteries, and is very important in evaluating the sustainability of the anode. In a typical cell, Li ions first move from the Li foil to the SCAu-CC collector, and deposit onto the collector. After that, Li is stripped and returns back to the Li foil. Furthermore, the CE can be affected by the current density and areal capacity. The CE of the cell using the SCAu-CC collector was investigated from specific charge/discharge profiles under conditions of a high current density of 4 mA cm^{-2} and considerable areal capacities of 10 and 12 mA h cm^{-2}, which exhibit excellent stability of the deeply cyclable Li plating/stripping behavior (Fig. 3c and S12†). Due to the decrease of the diameter and increase of the surface atoms, the evenly distributed single-cluster Au can improve surface activity, which presents higher

reactivity for adsorption of Li ions. In addition, single-cluster Au may enhance the rate of electron transport while influencing the structural stability of the material, both effects potentially leading to enhanced surface reactivity. The SCAu-CC collector exhibited a stable CE with a high areal capacity of 15 mA h cm^{-2} during the deep charge–discharge cycles. The CE of the SCAu-CC collector was also evaluated by continuously varying current densities. Fig. 3d shows that the CE varies by about 99.91–99.17% when the current density is varied from 0.5 to 5.0 mA cm^{-2} corresponding to an areal capacity from 1.0 to 10.0 mA h cm^{-2}. Even at a high current density of 7.5 and 10.0 mA cm^{-2} corresponding to an areal capacity of 15.0 and 20.0 mA h cm^{-2}, respectively, it is still capable of retaining a high and stable CE of 98.23% and 95.90%. This shows that the electrodes in this study can realize deep cycling and much higher capacities without compromising other properties such as the CE and cycle life, which is suitable for commercial applications in quick-charging systems.

As shown in Fig. 3e, the average CE is about 99.82% for 900 cycles at a current density of 0.5 mA cm^{-2} with an areal capacity of 1.0 mA h cm^{-2}. In contrast, batteries using the CC collector exhibit a stable CE of 99.3% for the initial 283 cycles, followed by fluctuating CEs, which could be attributed to the reaction of the electrolyte with exposed Li metal to re-form the SEI layer during the repeated lithium deposition/dissolution process. A similar CE performance is achieved at a current density of 1.0 mA cm^{-2} with an areal capacity of 2.0 mA h cm^{-2} (Fig. S14†). In addition, at a high current density of 3.0 mA cm^{-2}, batteries using the CC collector exhibit a rapid decay of the CE to less than 88.4% after 21 cycles. Fluctuating CEs are observed for the PAu-CC collector after 50 cycles. The CEs of SCAu-CC can remain stable at 99.23% for over 80 cycles at a deposition areal capacity of 6.0 mA h cm^{-2} (Fig. 3f). Under even harsher conditions at a high current density of 4.0 mA cm^{-2} with an areal capacity of 10.0 mA h cm^{-2}, batteries with the SCAu-CC collector can work stably with high average CEs of 99.16%. The excellent cycling stability and high coulombic efficiency encourage us to investigate their fast-charging capability, which is a key enabler of major parameters for electric vehicles. Here, the fast-charging capability of SCAu-CC was investigated at a high current density of 4.0 mA cm^{-2} with an areal capacity of 1.0 mA h cm^{-2}. As shown in Fig. S15,† the average coulombic efficiency of our strategy can reach up to 99.4%.

To further study the electrochemical behavior, Li||Li, Li-CC||CC-Li, Li-PAu-CC||CC-PAu-Li and Li-SCAu-CC||SCAu-CC-Li symmetrical cells were configured for testing (Fig. 3g). At a current density of 2.0 mA cm^{-2} and a capacity of 1.0 mA h cm^{-2}, the Li||Li cell exhibits much worse performance with random voltage oscillations and a large overpotential of >168 mV followed by continuous overpotential increases during the repeat cycles. The dendrite-induced short circuit occurs within 70 h, signaled by voltage fluctuations.[31–33] Similarly, the Li-CC||CC-Li symmetrical cell shows a fluctuating overpotential of 120.0 mV, and the Li-PAu-CC||CC-PAu-Li cell shows a high overpotential of 89.8 mV with a voltage increase after cycling for 220 h, indicating uneven Li deposition. In contrast, the Li-SCAu-CC||SCAu-CC-Li cell displayed an excellent cycling stability as evidenced by a much lower overpotential, which further stabilized at 37.0 mV for more than 500 h. From Fig. S16,† the overpotential of Li||Li, Li-CC||CC-Li and Li-PAu-CC||CC-PAu-Li symmetric cells presents an obvious wave phenomenon at a higher current density of 3.0 mA cm^{-2}, but the Li-SCAu-CC||CC-SCAu-Li cell exhibits stable voltage profiles for over 350 h. All the above phenomena illustrate that as the nucleation

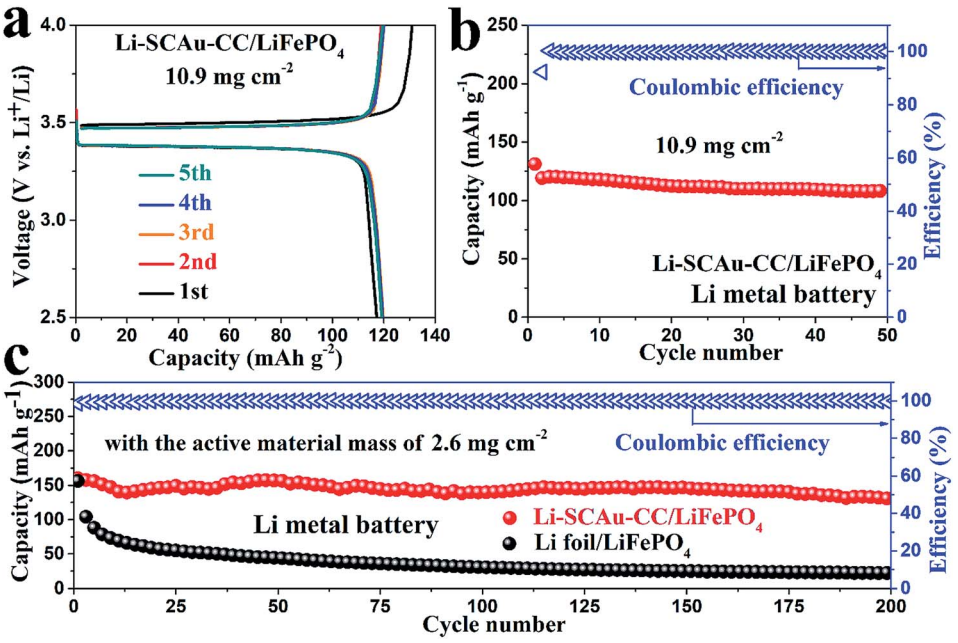

Fig. 4 High Li metal utilization. (a) Galvanostatic charge–discharge profiles and (b) cycling performance of Li-SCAu-CC/$LiFePO_4$ metal batteries with an active material loading of up to 10.9 mg cm^{-2}. (c) Long-term cycling performance of Li metal batteries.

and growth of Li metal are seeded by single-cluster Au, Li metal can be deposited on the carbon skeleton uniformly and reversibly, which can mitigate the degradation of Li metal upon cycling.

To further demonstrate the advantages of the SCAu-CC collector, we conducted a proof-of-concept study on LMBs assembled with Li-SCAu-CC as anodes and $LiFePO_4$ as cathodes. The Li-SCAu-CC anodes were prepared by the predeposition of Li onto the SCAu-CC electrode. The battery with a cathode active material mass of 10.9 mg cm^{-2} was galvanostatically cycled between 2.5 and 4.0 V to study its specific capacities to gain a better understanding of Li utilization and commercially sustainable development of the Li-SCAu-CC anode. As illustrated schematically in Fig. 4a, each profile shows charge/discharge voltage plateaus, corresponding to the two-phase reaction of Li extraction and insertion, which is in agreement with the traditional $LiFePO_4$ cell. At a current density of 0.1C (1.0C = 170 mA g^{-1}), the cell delivers capacities of 124.3 mA h g^{-1} with an average CE of 99.6% during cycling (Fig. 4b), thereby satisfying the requirements for commercial manufacturing. Furthermore, the cell exhibits a very stable cycling performance with an active material mass of 2.6 mg cm^{-2} over 200 cycles as shown in Fig. 4c. The specific capacity shows an initial value of 161.5 mA h g^{-1} with a tiny capacity reduction of 0.14% per cycle, which was very close to its theoretical value, and the CE approached 99.86% during each cycle.

Conclusions

In summary, single-cluster Au dispersed on a functionalized carbon skeleton is used to induce substrate-dependent metal nucleation processes during its electrochemical plating, on which Li metal is guided to form a smooth Li metal anode without dendrites. DFT calculations and *in situ* optical microscopy observations are used to reveal the guiding function between single-cluster Au and Li metal. The resulting Li anode exhibits excellent cycling stability up to 900 cycles and is deeply cyclable to high capacities of 20.0 mA h cm^{-2}. Cells with $LiFePO_4$ cathodes show the feasibility of the anodes with excellent cycling stability up to 200 cycles, which benefits from guided deposition and high Li metal utilization. We believe that with continuous efforts, single clusters or atoms will play an important role in modified current collectors of alkali metal batteries in consideration of both Li metal deposition and utilization, towards the realization of large-scale energy storage applications.

Conflicts of interest

There are no conflicts to declare.

Acknowledgements

F. R. is grateful to the Canada Research Chairs program for partial salary support and acknowledges funding from the Natural Sciences and Engineering Research Council of Canada (NSERC) for a Discovering Grant and the Canada Foundation for Innovation (CFI) for infrastructure support and operating funds. C. Y. acknowledges funding from the National Natural Science Foundation of China (no. 51402202), the Jiangsu Shuangchuang Plan, and the Priority Academic Program Development of Jiangsu Higher Education Institutions (PAPD). T. Y. acknowledges the Fonds de recherche du Québec-Nature et technologies (FRQNT) for a personal fellowship.

Notes and references

1 M. Armand and J.-M. Tarascon, *Nature*, 2008, **451**, 652–657.
2 J. Sun, H.-W. Lee, M. Pasta, H. Yuan, G. Zheng, Y. Sun, Y. Li and Y. Cui, *Nat. Nanotechnol.*, 2015, **10**, 980–985.
3 P. G. Bruce, S. A. Freunberger, L. J. Hardwick and J.-M. Tarascon, *Nat. Mater.*, 2011, **11**, 19–29.
4 Z. Peng, S. A. Freunberger, Y. Chen and P. G. Bruce, *Science*, 2012, **337**, 563–566.
5 W. Li, Z. Yang, M. Li, Y. Jiang, X. Wei, X. Zhong, L. Gu and Y. Yu, *Nano Lett.*, 2016, **16**, 1546–1553.
6 Y. Zhao, K. R. Adair and X. Sun, *Energy Environ. Sci.*, 2018, **11**, 2673–2695.
7 Y. Zhang, W. Luo, C. Wang, Y. Li, C. Chen, J. Song, J. Dai, E. M. Hitz, S. Xu, C. Yang, Y. Wang and L. Hu, *Proc. Natl. Acad. Sci. U. S. A.*, 2017, **114**, 3584–3589.
8 C. Yang, H. Xie, W. Ping, K. Fu, B. Liu, J. Rao, J. Dai, C. Wang, G. Pastel and L. Hu, *Adv. Mater.*, 2019, **31**, e1804815.
9 P. J. Kim and V. G. Pol, *Adv. Energy Mater.*, 2018, **8**, 1802665.
10 Y. Zhang, C. Wang, G. Pastel, Y. Kuang, H. Xie, Y. Li, B. Liu, W. Luo, C. Chen and L. Hu, *Adv. Energy Mater.*, 2018, **8**, 1800635.
11 J. Zhao, G. Zhou, K. Yan, J. Xie, Y. Li, L. Liao, Y. Jin, K. Liu, P.-C. Hsu, J. Wang, H.-M. Cheng and Y. Cui, *Nat. Nanotechnol.*, 2017, **12**, 993–999.
12 Z. Tu, S. Choudhury, M. J. Zachman, S. Wei, K. Zhang, L. F. Kourkoutis and L. A. Archer, *Nat. Energy*, 2018, **3**, 310–316.
13 X. Chen, X. Shen, B. Li, H.-J. Peng, X.-B. Cheng, B.-Q. Li, X.-Q. Zhang, J.-Q. Huang and Q. Zhang, *Angew. Chem.*, 2018, **57**, 734–737.
14 R. Zhang, X. Chen, X. Shen, X.-Q. Zhang, X.-R. Chen, X.-B. Cheng, C. Yan, C.-Z. Zhao and Q. Zhang, *Joule*, 2018, **2**, 764–777.
15 C. Yang, K. Fu, Y. Zhang, E. Hitz and L. Hu, *Adv. Mater.*, 2017, **29**, 1701169.
16 Q. Shi, Y. Zhong, M. Wu, H. Wang and H. Wang, *Proc. Natl. Acad. Sci. U. S. A.*, 2018, **115**, 5676–5680.
17 Z. Sun, S. Jin, H. Jin, Z. Du, Y. Zhu, A. Cao, H. Ji and L.-J. Wan, *Adv. Mater.*, 2018, **30**, e1800884.
18 C. Yang, Y. Yao, S. He, H. Xie, E. Hitz and L. Hu, *Adv. Mater.*, 2017, **29**, 1702714.
19 K. Yan, Z. Lu, H.-W. Lee, F. Xiong, P.-C. Hsu, Y. Li, J. Zhao, S. Chu and Y. Cui, *Nat. Energy*, 2016, **1**, 16010.
20 J. Pu, J. Li, Z. Shen, C. Zhong, J. Liu, H. Ma, J. Zhu, H. Zhang and P. V. Braun, *Adv. Funct. Mater.*, 2018, **42**, 1804133.
21 X.-L. Ma, J.-C. Liu, H. Xiao and J. Li, *J. Am. Chem. Soc.*, 2018, **140**, 46–49.
22 L. Liu and A. Corma, *Chem. Rev.*, 2018, **118**, 4981–5079.

23 X. Li, W. Bi, L. Zhang, S. Tao, W. Chu, Q. Zhang, Y. Luo, C. Wu and Y. Xie, *Adv. Mater.*, 2016, **28**, 2427–2431.
24 J.-C. Liu, X.-L. Ma, Y. Li, Y.-G. Wang, H. Xiao and J. Li, *Nat. Commun.*, 2018, **9**, 1610.
25 X.-F. Yang, A. Wang, B. Qiao, J. Li, J. Liu and T. Zhang, *Acc. Chem. Res.*, 2013, **46**, 1740–1748.
26 J. Zhang, J. Liu, L. Xi, Y. Yu, N. Chen, S. Sun, W. Wang, K. M. Lange and B. Zhang, *J. Am. Chem. Soc.*, 2018, **140**, 3876–3879.
27 H. Wei, X. Liu, A. Wang, L. Zhang, B. Qiao, X. Yang, Y. Huang, S. Miao, J. Liu and T. Zhang, *Nat. Commun.*, 2014, **5**, 5634.
28 N. Cheng, S. Stambula, D. Wang, M. N. Banis, J. Liu, A. Riese, B. Xiao, R. Li, T.-K. Sham, L.-M. Liu, G. A. Botton and X. Sun, *Nat. Commun.*, 2016, **7**, 13638.
29 R. Zhang, X.-R. Chen, X. Chen, X.-B. Cheng, X.-Q. Zhang, C. Yan and Q. Zhang, *Angew. Chem.*, 2017, **129**, 7872–7876.
30 L. Guo and P. C. Searson, *Electrochim. Acta*, 2010, **55**, 4086–4091.
31 K. N. Wood, M. Noked and N. P. Dasgupta, *ACS Energy Lett.*, 2017, **2**, 664–672.
32 K. H. Chen, K. N. Wood, E. Kazyak, W. S. LePage, A. L. Davis, A. J. Sanchez and N. P. Dasgupta, *J. Mater. Chem. A*, 2017, **5**, 11671–11681.
33 E. Kazyak, K. N. Wood and N. P. Dasgupta, *Chem. Mater.*, 2015, **27**, 6457–6462.